Acta Materialia 184 (2020) 143–150

Contents lists available at ScienceDirect

Acta Materialia

journal homepage: www.elsevier.com/locate/actamat

Full length article

Synthesis of α''-$Fe_{16}N_2$ foils with an ultralow temperature coefficient of coercivity for rare-earth-free magnets

Jinming Liu[a], Guannan Guo[a], Xiaowei Zhang[b], Fan Zhang[a], Bin Ma[a], Jian-Ping Wang[a,*]

[a] Department of Electrical and Computer Engineering, University of Minnesota, 200 Union St SE, Minneapolis, MN 55455, USA
[b] Niron Magnetics, 650 Taft St NE #400, Minneapolis, MN 55413, USA

ARTICLE INFO

Article history:
Received 24 September 2019
Revised 12 November 2019
Accepted 19 November 2019
Available online 25 November 2019

Keywords:
α''-$Fe_{16}N_2$ foils
Rare-earth-free magnets
Permanent magnet
Low-temperature nitridation
Porous structure

ABSTRACT

Magnets with a low-temperature coefficient of coercivity (TCC) have various applications in a varying temperature environment. Rare-earth magnets like NdFeB are widely used, but they usually have a large negative TCC. Here, it is first experimentally demonstrated that α''-$Fe_{16}N_2$ foils, as a candidate for rare-earth-free magnets, have an ultralow positive TCC (0.4 Oe/K) from 300 K to 425 K. It is two orders of magnitude smaller than that of the commercial NdFeB magnets in this temperature range. The α''-$Fe_{16}N_2$ foils are made from as-rolled iron foils (25 μm) by a low-temperature nitridation process (< 473 K). The microstructure of these iron foils is tuned before the nitridation by a combined oxidation and reduction process to induce pores and defects that could significantly enhance the diffusivity of nitrogen atoms in the foils. The fabricated α''-$Fe_{16}N_2$ foils exhibit the specific saturation magnetization up to 222 emu/g at 300 K (reduced iron foils ~ 205 emu/g) and the coercivity 1.1 kOe. The synthesized α''-$Fe_{16}N_2$ foils have an ultralow TCC and a high saturation magnetization besides its usages of low-cost and environment-friendly raw materials. These combined unique features make α''-$Fe_{16}N_2$ a promising rare-earth-free alternative for many applications required less temperature dependence of magnetic properties.

1. Introduction

Rare-earth magnets such as NdFeB are widely used in various industrial products such as mobile phones, electronic motors, and wind turbines [1–4] The high cost and concerns on environmental degradation of the rare-earth elements stimulate the research work on alternative rare-earth-free magnets [5–7]. Several excellent reviews showed the potential candidates of rare-earth-free magnets, such as MnAl, MnBi, Alnico, $L1_0$ FeNi, $L1_0$ FeCo, cobalt-based alloys, carbides, and iron nitride (α''-$Fe_{16}N_2$) [7–9]. Among them, α''-$Fe_{16}N_2$ is getting considerable interests from both academia and industry due to its giant saturation magnetization (M_s ~2.9 T (~305 emu/g)), which is even larger than FeCo alloys [10,11], and relatively high magnetocrystalline anisotropy (>1.0 × 10^7 erg/cm^3) [12–16]. The raw materials of α''-$Fe_{16}N_2$, Fe and N, are environment-friendly and also convenient to obtain for mass production, which can dramatically reduce the manufacturing and environmental cost. α''-$Fe_{16}N_2$ has a body-centered tetragonal structure with N atoms orderly occupying octahedral interstices [17]. The tetragonally distorted iron itself could also show high magnetic anisotropy due to the structural asymmetry [18,19]. Considerable research efforts have been devoted to synthesizing α''-$Fe_{16}N_2$ nanoparticles (NPs) and powders in past decades [12,20–24]. Importantly, thin α''-$Fe_{16}N_2$ foils (~0.5 μm) with H_c~1.9 kOe and a maximum magnetic energy product up to 20 MGOe at room temperature has been reported using an ion-implantation method [25].

Magnets with a low-temperature coefficient of coercivity are also attracting intense research interests because of the demands on the applications at varying temperatures, such as the high-performance audio devices (e.g., cell phone speakers and smart speakers), low-noise fans and microwave devices [26–28]. Rare-earth magnets like NdFeB, however, usually show a large negative temperature coefficient of coercivity, which may cause instability of the magnetic performances (lower H_c and energy product) when working at an elevated temperature. For example, the maximum energy product ($(BH)_{max}$) of a NdFeB magnet (N45) could decrease ~ 45% when the temperature increases from 300 K to 425 K [7]. This is because the coercivity of the NdFeB magnet decreases dramatically at that temperature range [29]. Therefore, magnets with a low and even positive temperature coefficient of coercivity should have advantages for the applications with varying temperatures. Ferrite magnets have a positive temperature coefficient of coercivity naturally. However, its saturation magnetiza-

* Corresponding author.
E-mail addresses: liux1872@umn.edu (J. Liu), jpwang@umn.edu (J.-P. Wang).

https://doi.org/10.1016/j.actamat.2019.11.052
1359-6454/

tion (M_s) is very low; thus, a low remanent magnetic flux density (B_r) is obtained. Magnets with low B_r will be requested with large volume for most of the magnet designs. As a contrast, the M_s of α''-$Fe_{16}N_2$ is two to four times larger than that of ferrite magnets. In this work, we discover that α''-$Fe_{16}N_2$ foils synthesized by a low-temperature nitridation method have an ultralow positive temperature coefficient of coercivity in the temperature range of 300–425 K. It indicates that α''-$Fe_{16}N_2$ is a promising candidate for rare-earth-free magnets, especially at elevated temperatures.

A low-temperature nitridation method was developed in the 1990s, which treated with iron nanoparticles (NPs) or reduced iron oxide NPs in ammonia gas at the temperature below 473 K, based on the Fe-N binary phase diagram [20,21]. It was reported that pure α''-$Fe_{16}N_2$ phase in the nitride NPs could be obtained by this method [30]. Interestingly, the low-temperature nitridation process using hydrogen-reduced iron oxide NPs showed a higher volume ratio of α''-$Fe_{16}N_2$ phase than using iron NPs. Micro-channels were introduced into the hydrogen-reduced iron oxide NPs, which helped improve the diffusivity of nitrogen atoms into the NPs during the consequent low-temperature nitridation process [23]. Kojima et al. recently used a leaching method to induce porous structure to iron-based alloy powders and enhance the nitridation efficiency at low temperature to form α''-$Fe_{16}N_2$ [31]. To reduce the magnetic interaction between α''-$Fe_{16}N_2$ NPs and enhance the coercivity, researchers introduced a nonmagnetic shell for the nitride NPs, such as Al_2O_3, SiO_2, etc. [22,32]. The saturation magnetization of the core-shell α''-$Fe_{16}N_2$ NPs, however, decreased due to the nonmagnetic shells. An external magnetic field was also used to align the orientation of α''-$Fe_{16}N_2$ NPs to enhance the remanence ratio and coercivity with the trade-off of reduced maximum energy product [33]. Many works of the low-temperature nitridation have so far focused on NPs due to its large surface to volume ratio and high nitrogen diffusivity. However, there are several remaining challenges for NPs to be made into bulk magnets, such as intrinsic low-packing-density and difficulty to handle and transfer, etc. In this sense, other bulk forms of raw materials such as thick foils and ribbons may help overcome these hurdles. Meanwhile, we realize that the diffusivity of nitrogen in foils is much smaller than that in NPs. This could be the main reason that there was no much progress along with this approach. Our strategy is that the microstructure of the foils should be tuned to enable the foils to be well-nitrided at the temperature lower than 473 K.

Tong et al. reported that the nitridation temperature of an iron plate (7 mm by 100 mm by 100 mm) decreased dramatically from more than 773 K to 573 K by generating nanograins in the sample using a surface mechanical attrition treatment. This method can obtain lots of micro-channels and defects into the iron plate and enhance the nitrogen diffusivity at a relatively low temperature [34]. We have also reported a successful synthesis of α''-$Fe_{16}N_2$ using 20 μm thick FeCuB ribbons as the starting material [35]. The FeCuB ribbons were first processed by oxidation, and hydrogen reduction. Then a porous structure was obtained for the ribbons, which enhanced the nitrogen diffusivity in the ribbon sample during the consequent low-temperature nitridation. Thus, α''-$Fe_{16}N_2$ ribbons with a porous structure were obtained. Some born oxides and copper clusters in the ribbon sample, however, downgraded the saturation magnetization of the nitride FeCuB ribbon significantly (~145 emu/g). Due to the complex effects of the copper and boron dopants on the microstructure of the ribbons, it was difficult to exclude the unnoticed effects of the copper clusters and boron nitrides in the nitridation process. It was challenging to investigate the materials systematically.

In this paper, we propose a method to tune the microstructure of iron foils (25 μm thick) by high-temperature oxidation (1248 K) and a hydrogen reduction process, making them suitable for the low-temperature nitridation to directly synthesize α''-$Fe_{16}N_2$ foils. Thick α''-$Fe_{16}N_2$ foils with high saturation magnetization (~222 emu/g) and relatively high coercivity (1.1 kOe) were obtained for the first time to our best knowledge. An ultralow temperature coefficient of coercivity (dH_c/dT~0.4 Oe/K) in those α''-$Fe_{16}N_2$ foils was observed in the temperature range from 300 K to 425 K, which outperforms NdFeB magnets. A bonded magnet was made out of α''-$Fe_{16}N_2$ foils with bonders.

2. Experimental procedure

High purity iron foils (Goodfellow, 25 μm, 99.99%) were used as the starting material to fabricate α''-$Fe_{16}N_2$ foils. There were three steps involved to prepare the α''-$Fe_{16}N_2$ foils: oxidation, hydrogen reduction, and low-temperature nitridation. A box furnace was used to oxidize the iron foils at the ambient condition at 1248 K for 5–30 min. The oxidized iron foils were reduced by pure hydrogen (99.999%) gas at 623 K in a tube furnace. The reduction helped get rid of the oxygen and induce a porous structure into the foils [35]. And then, the reduced foils were processed the low-temperature nitridation in the same tube furnace at 393~443 K, using dry ammonia gas (99.999%) as the nitrogen source. The nitriding potential, the partial pressure of the ammonia over that of hydrogen $p(NH_3)/p(H_2)^{3/2}$ [36], is adjusted by the ammonia gas flow rate and the temperature. A passivation process was followed by the low-temperature nitridation using a mixed gas of 1% O_2 and 99% Ar. The α''-$Fe_{16}N_2$ foils prepared by the low-temperature nitridation method could be used to prepare a bonded magnet by simply stacking the foils with bonders (glues). More details of the processing processes summarized in Fig. 1.

The crystalline structure, microstructures, chemical compositions, and magnetic properties were investigated. X-ray diffraction (XRD) patterns were collected to get the crystalline structures. The microstructures and chemical compositions were characterized by a scanning electron microscope (SEM), a high-resolution transmission electron microscopy (HRTEM), and scanning transmission electron microscopy (STEM). The magnetic properties were measured using a vibrating sample magnetometer (VSM) and a physical property measurement system (PPMS).

3. Results and discussion

3.1. Crystal structure analysis

The crystalline structure of the foils at different steps was characterized, as shown in Fig. 2. The x-ray diffraction (XRD) patterns of raw foil, oxidized foil, and reduced foil are labeled as a, b, and c, respectively. The highest diffraction peak of the raw foil is bcc Fe (211), around 82.3°, instead of (110), around 44.7° from the powder diffraction files. It indicates that the raw iron foil has a texture. After oxidation, the dominant phase of the foil is α-Fe_2O_3 hematite with some Fe_3O_4 magnetite. The saturation magnetization of the oxidized foil decreases dramatically as expected, which could be found in the following section. A hydrogen reduction process was applied to the oxidized foils in order to remove the oxygen and induce a porous structure in the foils. The diffraction pattern of the hydrogen-reduced foil, however, is similar to the powder diffraction patterns, where bcc Fe(110) is the highest diffraction peak. Thus, after the oxidation and reduction processes, the texture of the raw iron foils was partially destroyed.

The low-temperature nitridation process was carried out on the hydrogen-reduced iron foils. Different nitridation temperatures 393~443 K and ammonia flow rates 40~80 sccm was used. Fig. 3 shows a typical XRD pattern of an iron foil after the low-temperature nitridation. The primary diffraction peak is at 42.7° (2θ) which is consistent with other reports of α''-$Fe_{16}N_2$ (202) diffraction peak [30,32]. Some bcc Fe is also observed, indicating

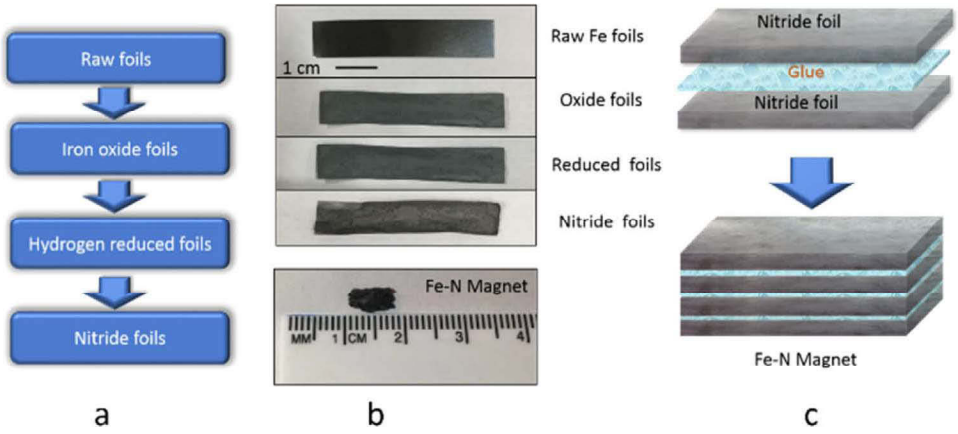

Fig. 1. Process steps of the low-temperature nitride α''- $Fe_{16}N_2$ foils. (a); raw iron foils were oxidized, reduced by hydrogen, and then processed the low-temperature nitridation. A Fe-N magnet could be made by stacking the α''- $Fe_{16}N_2$ foils. Photo of the foils at each step is shown (b); schematic drawing of making Fe-N magnets using nitride foils and bonders (glue) (c). (For interpretation of the references to colour in this figure legend, the reader is referred to the web version of this article.)

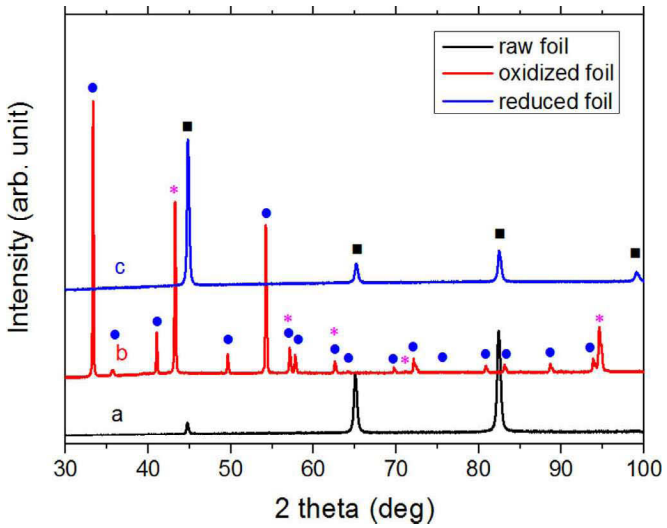

Fig. 2. XRD patterns of raw iron foil (25 μm thick) (a), oxidized foil after a 1248 K oxidation in a box furnace in the air (b), and reduced foil after performing a hydrogen-reduction at 623 K in a tube furnace on the oxidized foil (c). α-Fe is denoted by black squares; hematite is indicated by blue circles; magnetite is denoted by magenta stars. (For interpretation of the references to colour in this figure legend, the reader is referred to the web version of this article.)

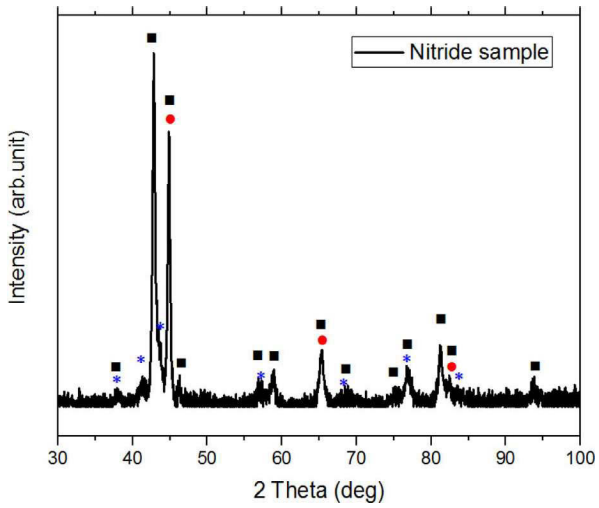

Fig. 3. A typical XRD pattern of the iron nitride foil. The nitridation was done on the hydrogen-reduced foil in the tube furnace at 423 K for 15 h. The α''-$Fe_{16}N_2$ phase was labeled by black squares; the Fe_3N over-nitride phase was marked by blue stars, and bcc Fe was labeled by red dots. (For interpretation of the references to colour in this figure legend, the reader is referred to the web version of this article.)

that there is residual bcc Fe in the nitride foil. There are also diffraction peaks, belongs to Fe_3N, the over-nitride phase, which was also confirmed by other researchers for the low-temperature nitridation method [12]. Generally, the over-nitride phase could be avoided by properly control the nitridation parameters.

3.2. Microstructure analysis

A scanning electron microscope (SEM) and a high-resolution transmission electron microscopy (HR-TEM) were used to characterize the microstructure of the nitride foils. Fig. 4a is an overview of the cross-sectional picture of the nitride foil sample. The thickness of the foil is around 50 μm, which is about two times thicker than that of the raw iron foil. The thickness enhancement is due to the formation of oxides during the oxidation process, in which the iron oxide grows both inward and outward of the original surface of an iron foil and makes the thickness of the foil around doubled [37]. The foil sample has a sandwich-like structure composed of three layers, which is contributed by the different oxide phases formed during the oxidation process, hematite at the outer regions and magnetite at the center part, respectively [37]. Both the outer region (Fig. 4b) and center part (Fig. 4c) have a porous structure, which creates open channels for nitrogen atoms to diffuse into the reduced iron foil much easier than the dense sample. In addition, during the reduction process, the removal of oxygen could leave vacancies/defects inside the grains, which helped nitrogen atoms easily diffuse into the iron grains and form α''-$Fe_{16}N_2$ phase. Zulhijah et al. [23] investigated the oxidation effect on the formation of α''-$Fe_{16}N_2$ phase using spherical core-shell α-Fe/Al_2O_3 nanoparticles. They found that when the nanoparticles were oxidized and then reduced by hydrogen, there were some so-called porous structures created in the NPs, which enhanced the low-temperature nitridation efficiency and α''-$Fe_{16}N_2$ phase volume ratio significantly in the nitride samples. For the Fe NPs treated by oxidation and consequent reduction, nitridation at 418 K for 15 h produced pure α''-$Fe_{16}N_2$ phase. For the NPs, however, without oxidation and reduction, longer nitridation time was required (~30–40 h), and the maximum α''-$Fe_{16}N_2$ phase volume ratio was ~82%.

It is similar in the hydrogen-reduced iron foil, where pores help nitrogen atoms diffuse more efficiently into the foil, and

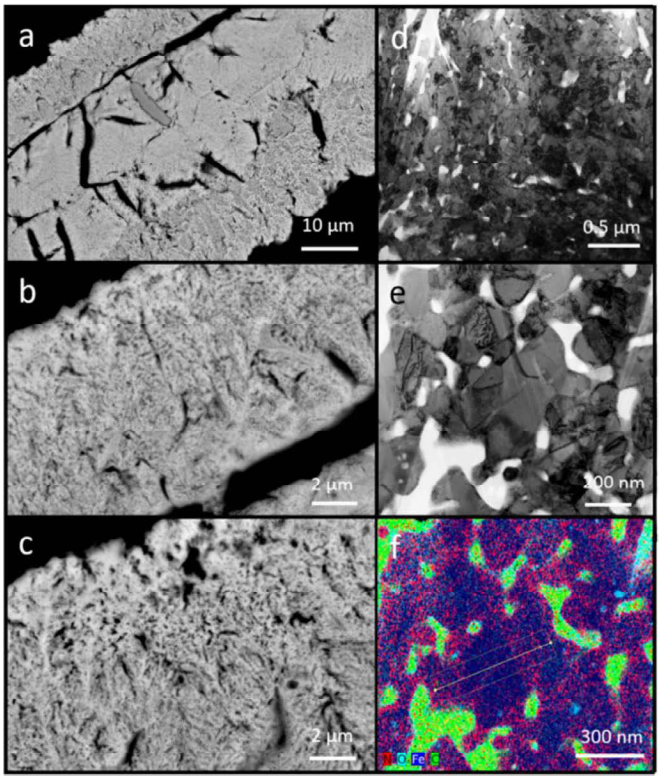

Fig. 4. The morphology and elemental mapping of the nitride foil after applying the nitridation on a hydrogen-reduced foil at 423 K for 15 h in the tube furnace, cross-sectional SEM images (a, b), and (c); TEM images (d), and (c); elemental mapping of N, O, Fe, and C corresponding to red, cyan, purple, and green respectively (f). (For interpretation of the references to colour in this figure legend, the reader is referred to the web version of this article.)

vacancies/defects in the grains made them easier to form α''-$Fe_{16}N_2$ phase during the low-temperature nitridation. Besides, iron foils without oxidation were also conducted following the low-temperature nitridation as experimental controls. It turns out that there is no α''-$Fe_{16}N_2$ phase detected for these control samples, but just bcc Fe is observed. This demonstrates the importance of the porous structure and vacancies/defects in the iron foils, which were introduced during the oxidation and reduction processes. A schematic model of the low-temperature nitridation process could be found in the supplementary information in figure S1.

The microstructure and chemical composition of the nitride sample were characterized using HR-TEM and scanning transmission electron microscopy (STEM) as revealed in Fig. 4d, e, and f. A porous structure is observed as shown in Fig. 4d, and e. During the preparation of TEM samples, polymers were filled into the porous regions of the foil sample to keep the original microstructure. The polymers would stay in the pores in the foil, and the pores could be easily detected. The size of the pores, providing open channels for nitrogen diffusion, is ranging from around 50 nm to hundreds nanometer. As illustrated in Fig. 4e, most of the grains of the nitride foil are in the range of 100 to 200 nm. The energy dispersive x-ray (EDX) data was also collected from the same region shown in Fig. 4e. Four different elements were characterized, N, O, Fe, and C. Carbon is from the polymers filled into the pores in the sample as discussed above, and the green regions (carbon regions) in Fig. 4f are consistent with the pores shown in Fig. 4e. As shown in Fig. 4f, nitrogen-rich regions are found close to the grain boundaries and the pores, where nitrogen atoms could quickly diffuse into the iron grains. In lager grains as denoted by a line in Fig. 4f, less nitrogen is detected in the central parts of the grains. It manifests that it is difficult for nitrogen to diffuse into the central parts of large grains and that there may be still some residual bcc Fe, which is consistent with the XRD results shown in Fig. 3. Smaller grains (less than 100 nm) with narrow size distribution are required to obtain a uniform nitride sample. The oxygen in the sample is from the passivation process (using a gas mixture 1% O_2+99% Ar) and/or the reaction between the nitride sample and air after taking the sample out of the tube furnace.

3.3. Analysis of magnetic properties

3.3.1. Magnetic characterizations

The hysteresis loops of a raw foil, oxidized foil, reduced foil, and nitride foil were measured as revealed in Fig. 5a. As we can see in the figure, the raw iron foil is magnetically soft with coercivity (H_c) less than 30 Oe. The saturation magnetization (M_s) of the raw iron foil is 215 emu/g. After the oxidation process at 1248 K in the air, the iron foil was oxidized. The M_s of the oxidized foil reduced dramatically, and H_c increased to ~ 70 Oe. After the hydrogen reduction, the M_s (~205 emu/g) of the sample recovered, but H_c was still small around 100 Oe. After the low-temperature nitridation, the hysteresis loop of the nitride foil was measured, as

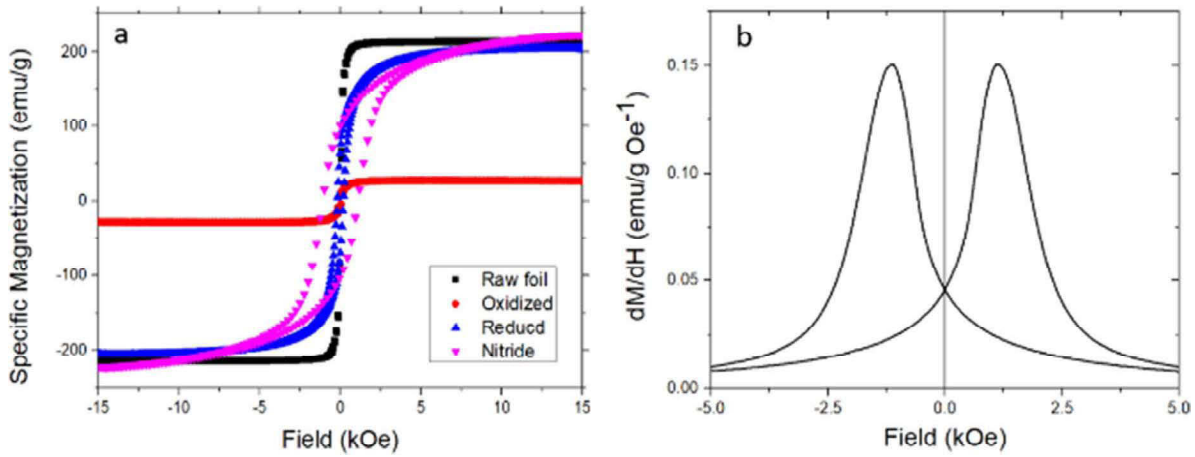

Fig. 5. (a) The hysteresis loop of raw iron foil (25 μm thick), oxidized foil after a 1248 K oxidation in a box furnace in air, reduced foil after performing a hydrogen-reduction at 623 K in the tube furnace on the oxidized foil, and nitride foil after applying the nitridation on a hydrogen-reduced foil at 423 K for 15 h in the tube furnace; (b) the first derivate of the hysteresis loop of the nitride foil shown in (a). (For interpretation of the references to colour in this figure legend, the reader is referred to the web version of this article.)

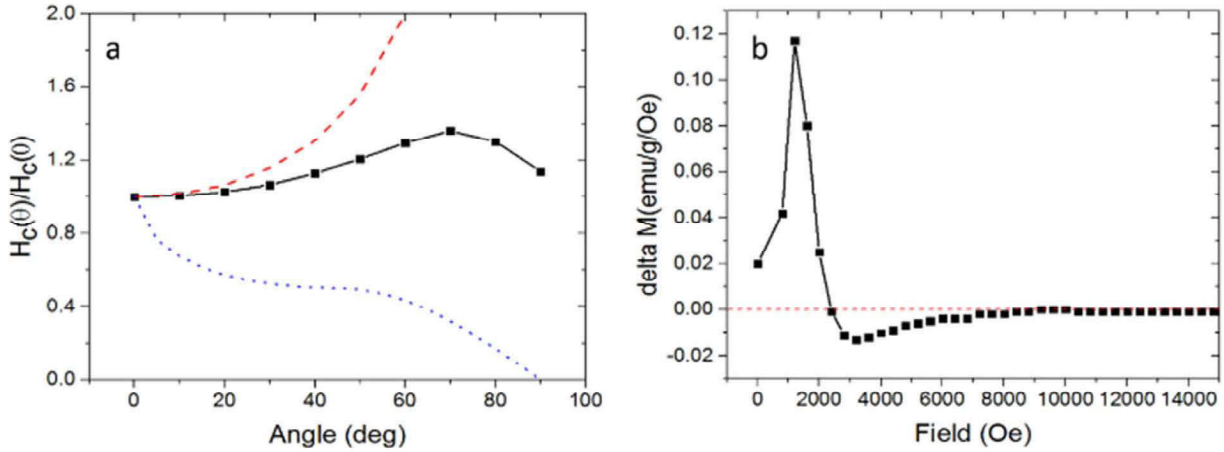

Fig. 6. (a) The angular dependence of coercivity of the nitride sample after applying the nitridation on a hydrogen-reduced foil at 423 K for 15 h in the tube furnace(black squares), Kondorski model (domain-wall motion, red dash line), and Stoner-Wohlfarth model (coherent rotation, blue dot line); (b) δ_M curve of the nitride sample shown in (a). (For interpretation of the references to colour in this figure legend, the reader is referred to the web version of this article.)

shown in Fig. 5a denoted by magenta triangles. The H_c enhanced significantly compared to the reduced sample, which could be attributed to the formation of α''-$Fe_{16}N_2$ in the nitride foil. Also, the M_s of nitride sample increases (222 emu/g) and is higher than that of the hydrogen-reduced foil and the raw foil, manifesting the high M_s of α''-$Fe_{16}N_2$ phase as reported by other researchers [12,30]. Since the nitride foil was passivated and may also partially oxidized in the air after being taken out from the tube furnace, the M_s of α''-$Fe_{16}N_2$ should be expected an even higher value than 222 emu/g. The H_c of the nitride foil is around 1.1 kOe. The first derivative of the hysteresis loop of the nitride foil was plotted in Fig. 5b to determine the switching field and switching field distribution. There are two symmetry peaks around ±1.1 kOe, which is similar to the H_c of the nitride foil. No other peaks were observed, indicating that α''-$Fe_{16}N_2$ grains exchange-coupled well with the retained bcc Fe grains. Otherwise, some other peaks at lower field range (<1.1 kOe) should be obtained since the coercivity of the reduced iron foil is very low (<100 Oe). The remanence ratio of the nitride foil is around 0.45 since the easy axes of α''-$Fe_{16}N_2$ grains are randomly oriented.

The orientation of grains could be tuned by a magnetic field. Watanabe et al. [38] demonstrated that aging of Fe-N alloy single crystals at 453 K in a magnetic field could align the orientation of the $Fe_{16}N_2$ precipitates. Jiang et al. [39] also reported recently that the phase constitution and crystalline orientation could be modified in a bulk FeN rod by post-annealing the sample in a 9 T magnetic field. Thus, applying a magnetic field during the low-temperature nitridation or post-annealing may help orientate the α''-$Fe_{16}N_2$ grains and eventually enhance the magnetic performance of the nitride foils.

The magnetic anisotropy of the nitride foils was estimated using the law of approach to saturation [40,41]. Nitride foils with different α''-$Fe_{16}N_2$ phase volume ratios were used for calculating the magnetic anisotropies. The anisotropy increases with the increase of α''-$Fe_{16}N_2$ phase volume ratio and enhances significantly when the α''-$Fe_{16}N_2$ phase ratio is higher than 50%, as shown in figure S2, indicating α''-$Fe_{16}N_2$ has higher magnetic anisotropy than that of bcc Fe. The anisotropy is ranging from 3×10^6 to 7×10^6 erg/cm^3 with the increase of α''-$Fe_{16}N_2$vol ratio. However, the anisotropy is smaller than the reported value ($>1 \times 10^7$ erg/cm^3), which could be due to the residual soft bcc Fe in the nitride foils. The exchange coupling between bcc Fe and α''-$Fe_{16}N_2$ leads to a lower effective magnetic anisotropy of the nitride foils. The details of the estimation of magnetic anisotropy of the nitride foils could be found in the supplementary information.

3.3.2. A model of the magnetization switching for nitride foils

To further understand the mechanism of magnetization switching of a nitride foil, we measured the angular dependence hysteresis loops, from in-plane (0°), parallel to the nitride foil plane, to out-of-plane (90°), perpendicular to the nitride foil plane, with 10° increment. The angular dependence H_c is shown in Fig. 6a. The $H_c(\theta)$, which represents the coercivity of different angles, was normalized to the H_c at 0°, H_c (0). The coercivity of the nitride foil keeps increasing from 0° to 70°, and then decreases sharply from 70° to 90°.

The magnetization reversal of magnetic materials may have different mechanisms such as a domain wall motion model (Kondorski model), and a coherent rotation model (Stoner–Wohlfarth model). In the Kondorski model, the dependence of coercivity versus the externally applied field for the ideal multidomain case could be expressed in the following relationship:

$$H_c(\theta) = H_c(0)/\cos\theta, \quad (1)$$

where θ denotes the angle between the external magnetic field and the easy-magnetization axis [42]. For the coherent rotation, Stoner-Wohlfarth model, the coercivity decreases down to zero with the angle increases from 0° to 90°. These two models are plotted in Fig. 6a, red dash line represents the predicted results obtained from Kondorski model, and blue dot line represents the Stoner–Wohlfarth model, respectively. For the nitride sample, the trend of the angular dependence coercivity is between these two models. Both domain wall motion and coherent rotation may occur in the sample at the same time, which could be attributed to the modified Kondorski model by adding the contribution of coherent rotation [43].

The difference of magnetization switching mechanisms between the dense and porous materials was investigated. Kasiuk et al. compared the magnetization reversal mechanism of continuous Co/Pd film on a silicon wafer and porous Co/Pd film on a porous thick-wall TiO_2 prepared by anodizing a Ti foil [42]. The $H_c(\theta)$ of the porous film sample keeps decreasing from 0 to 90°, which can be corresponded to the rotation of magnetic moments. In this case, the domain-wall motion is not the dominant mechanism because the sample has a network structure with partially isolated toroid-like grains. The $H_c(\theta)$ of the dense film, however, has a similar trend to that observed for the iron nitride foil sample, where $H_c(\theta)$ increases from 0°–70° and then decreases sharply from 70°–90°.

A modified Kondorski model containing the combined contributions of domain-wall motion and coherent rotation was proposed, which matched the experimental data. We believe that the

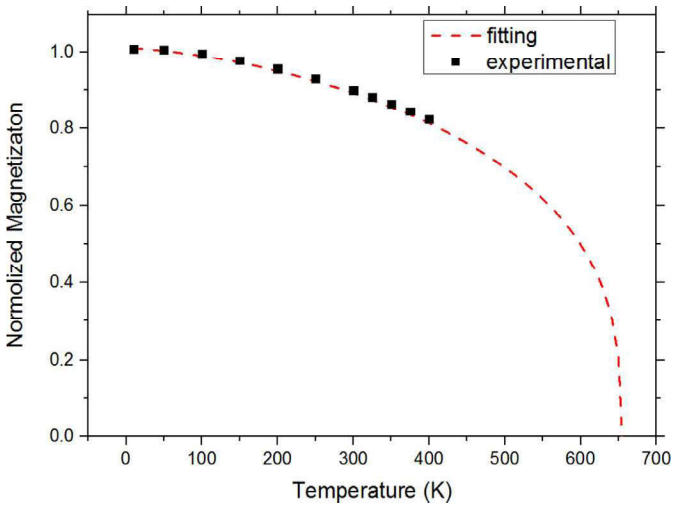

Fig. 7. The temperature-dependent saturation magnetization M_s of the nitride sample after a nitridation (150 C, 15 h) on a hydrogen reduced foil in the tube furnace (black squares) and the fitting data (red dash line) are based on the Eq. (4). (For interpretation of the references to colour in this figure legend, the reader is referred to the web version of this article.)

magnetization reversal mechanism of the nitride foil sample should also follow a similar modified Kondorski model. Based on this analysis, the H_c of the nitride foil sample could further be increased by isolating the grains to enhance the contribution of coherent rotation.

Magnetic interactions between grains of the nitride foil sample were also investigated by characterizing the remanent curves, Isothermal Remanent Demagnetization (IRM) curve, and Direct Current Demagnetization (DCD) curve. If magnetic grains have uniaxial anisotropy and there are no magnetic interactions among them, the two remanent values (IRM, DCD) should follow the following relation: [44,45]

$$M_{DCD}(H) = 1 - 2M_{IRM}(H) \quad (2)$$

The Eq. (2) could be modified as follows:

$$\delta M(H) = M_{DCD}(H) - (1 - 2M_{IRM}(H)), \quad (3)$$

in which δ_M equal to zero indicates that there is no interaction among the magnetic grains. Any value other than zero is due to the presence of magnetic interaction in the system, either exchange interaction for the positive value or dipolar interaction for the negative case. The δ_M plot of the nitride foil sample is shown in Fig. 6b. The plot shows the existence of strong exchange interactions in the magnetic field range smaller than 2 kOe. The large exchange interaction between these magnetic grains makes the grains magnetically coupled together. Then the domain wall motion is the major magnetization reversal mechanism, which led to the low H_c.

3.3.3. Curie temperature of nitride foils

The Curie temperature (T_C) of the nitride foil sample was estimated by fitting the temperature-dependent saturation magnetization from 10 K to 400 K, where the α''-$Fe_{16}N_2$ phase is thermally stable. Kuz'min proposed an equation (Eq. (4)) [46] to estimate the T_C, which follows Bloth's 3/2 power at the low-temperature range and 1/3 power of the Heisenberg model close to the critical region. In the equation $m = M_s/M_0$ (M_0: the M_s at 0 K), $\tau = T/T_C$, s and p are fitting parameters.

$$m(\tau) = \left[1 - s\tau^{3/2} - (1-s)\tau^{p}\right]^{1/3} \quad (4)$$

The T_C of the nitride foil sample was estimated to be 653 K, by fitting the M_s vs. T data using Eq. (4), as shown in Fig. 7. T_C of α''-$Fe_{16}N_2$ thin film was calculated as 813 K by Sugita et al. [47] using the Langevin function, which might overestimate the T_C since the mean-field model was used for the calculation [48]. Dirba et al. also reported the T_C of α''-$Fe_{16}N_2$ nanoparticles, which was 634 K, using the Eq. (4), which was close to the T_C obtained for the nitride foil sample [12].

3.3.4. Temperature-dependent magnetic properties of nitride foils

Magnets with a positive coefficient of coercivity are preferred for applications at various temperatures such as traction motors

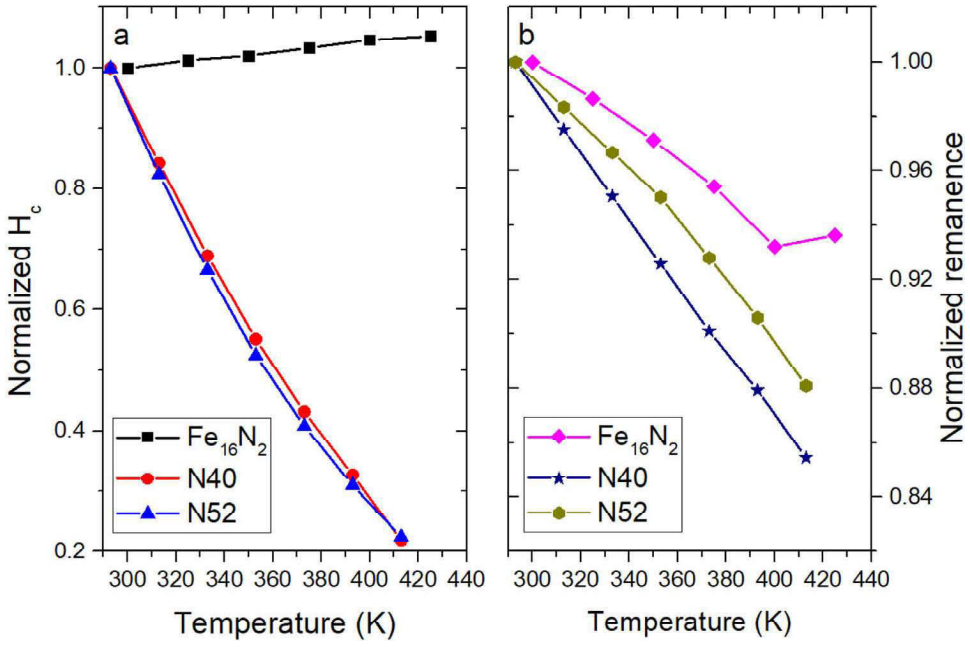

Fig. 8. Temperature-dependent magnetic properties of $Fe_{16}N_2$ low-temperature nitride foil and NdFeB magnets N40 and N52 (N40 and N52, data from the company TC-MAG, https://www.r4ymagnetics.com/Demagnetized-Curves-of-Neodymium-Magnets.htm); (a) the temperature-dependent coercivity of $Fe_{16}N_2$ and NdFeB magnets; (b) the temperature-dependent remanence of these two materials.

for electric vehicles. Hysteresis loops of the nitride foil were measured from 300 K to 425 K to evaluate the thermal stability of α''-$Fe_{16}N_2$. Remarkably, a positive temperature coefficient of coercivity (dH_c/dT~0.4 Oe/K from 300 K-425 K) of the nitride foil was obtained. The H_c increases slightly with temperature from 300 K up to 425 K, as shown in Fig. 8a (black squares). The slight increase of H_c for the nitride foil might be due to the slower decreasing rate of its magnetic anisotropy than its saturation magnetization in this temperature range. This may lead to a slightly higher magnetic switching field based on the Stoner-Wohlfarth model. We also compare the temperature-dependent H_c of commercial NdFeB magnets (N40 and N52, data from the company TCMAG, https://www.r4ymagnetics.com/Demagnetized-Curves-of-Neodymium-Magnets.htm) with the nitride foil. These data were also added into Fig. 8a (red dots for the N40 magnet (dH_c/dT ~ −81.9 Oe/K), and blue triangles for N52 magnet (dH_c/dT ~ −73.1 Oe/K)). We normalized the H_c of these samples for an easier comparison, where the H_c of the nitride foil sample was normalized to H_c(300 K), and H_c of NdFeB magnets to H_c(293 K). As shown in Fig. 8a, the temperature-dependent coercivity of α''-$Fe_{16}N_2$ is much more stable than that of NdFeB magnets. Furthermore, the temperature-dependent of magnetic remanence of the nitride foil and NdFeB magnets were also compared as revealed in Fig. 8b. These data were also normalized for the comparison. For the nitride foil sample, the magnetic remanence was normalized to the remanence at 300 K, and NdFeB magnets were normalized to the remanence at 293 K. The remanence of NdFeB magnets also decreases faster with temperature than that of the nitride foil sample. Thus, as a candidate of a rare-earth-free magnet, $Fe_{16}N_2$ has better temperature-dependent stability than NdFeB in the temperature ranging from 300 K to 425 K.

4. Conclusion

Iron foils (25 μm) was used as the starting raw material to fabricate α''-$Fe_{16}N_2$ by a low-temperature nitridation method. A porous structure was introduced into the iron foil by the oxidation and hydrogen reduction process, which was the key to obtain a porous nitride foil with a high α''-$Fe_{16}N_2$ phase ratio in the foil samples. The saturation magnetization of the nitride foil is around 222 emu/g higher than the reduced iron foil (~205 emu/g). Its coercivity is around 1.1 kOe, which could be further enhanced by reducing the exchange interactions between grains of the nitride foil. The effective magnetic anisotropy of the nitride sample is up to 7×10^6 erg/cm^3, increasing with the phase volume ratio of α''-$Fe_{16}N_2$. The relatively low effective magnetic anisotropy constant is due to the retained bcc Fe. Curie temperature of the nitride foil is around 653 K close to that of the α''-$Fe_{16}N_2$ nanoparticle samples. The low-temperature nitride α''-$Fe_{16}N_2$ foil shows a positive temperature coefficient of coercivity from 300 K to 425 K, which makes α''-$Fe_{16}N_2$ foil a promising candidate for rare-earth-free magnets. A bonded magnet could be made by stacking the $Fe_{16}N_2$ foils with bonders. Future research could focus on obtaining higher α''-$Fe_{16}N_2$ phase volume ratio, reducing the exchange interactions between grains, and aligning the easy axes of the grains.

Declaration of Competing Interest

Dr. Jian-Ping Wang has equity and royalty interests in and serves on the Board of Directors, for Niron Magnetics Inc, a company involved in the commercialization of FeN magnet. The University of Minnesota also has equity and royalty interests in Niron Magnetics Inc. These interests have been reviewed and managed by the University of Minnesota in accordance with its Conflict of Interest policies.

Acknowledgement

Part of this work was carried out in the Characterization Facility, the University of Minnesota, which receives partial support from NSF through the MRSEC program. Authors also thank the partial support from the Institute for Rock Magnetism, Department of Earth Science, the University of Minnesota for the use of instruments. We are grateful to Dr. John Larson, Dr. Frank Johnson, Mr. Rich Greger, and Mr. Chad from Niron Magnetics Inc. For their help in foil preparation.

Supplementary materials

Supplementary material associated with this article can be found, in the online version, at doi:10.1016/j.actamat.2019.11.052.

References

[1] D. Prosperi, A.I. Bevan, G. Ugalde, C.O. Tudor, G. Furlan, S. Dove, P. Lucia, M. Zakotnik, Performance comparison of motors fitted with magnet-to-magnet recycled or conventionally manufactured sintered NDFEB, J. Magn. Magn. Mater. 460 (2018) 448–453, doi:10.1016/j.jmmm.2018.04.034.
[2] H. Chen, X. Yang, L. Sun, P. Yu, X. Zhang, L. Luo, Effects of Ag on the magnetic and mechanical properties of sintered NDFEB permanent magnets, J. Magn. Magn. Mater. 485 (2019) 49–53, doi:10.1016/j.jmmm.2019.04.071.
[3] S. Chu, A. Majumdar, Opportunities and challenges for a sustainable energy future, Nature 488 (2012) 294–303, doi:10.1038/nature11475.
[4] J.M.D. Coey, Permanent magnet applications, J. Magn. Magn. Mater. 248 (2002) 441–456, doi:10.1016/S0304-8853(02)00335-9.
[5] B.J. Smith, R.G. Eggert, Costs, substitution, and material use: the case of rare earth magnets, Environ. Sci. Technol. 52 (2018) 3803–3811, doi:10.1021/acs.est.7b05495.
[6] J.-R. Riba, C. López-Torres, L. Romeral, A. Garcia, Rare-earth-free propulsion motors for electric vehicles: a technology review, Renew. Sustain. Energy Rev. 57 (2016) 367–379, doi:10.1016/j.rser.2015.12.121.
[7] J. Cui, M. Kramer, L. Zhou, F. Liu, A. Gabay, G. Hadjipanayis, B. Balasubramanian, D. Sellmyer, Current progress and future challenges in rare-earth-free permanent magnets, Acta Mater. 158 (2018) 118–137, doi:10.1016/j.actamat.2018.07.049.
[8] J.P Wang, Environment-friendly bulk $Fe_{16}N_2$ permanent magnet: Review and perspective, J. Magn. Magn. Mater. doi10.1016/j.jmmm.2019.165962.
[9] M. Mehedi, Y. Jiang, B. Ma, J.P. Wang, Nitriding and martensitic phase transformation of the copper and boron doped iron nitride magnet, Acta Mater. 167 (2019) 80–88, doi:10.1016/j.actamat.2019.01.034.
[10] N. Ji, X. Liu, J.-P. Wang, Theory of giant saturation magnetization in α''-$Fe_{16}N_2$: role of partial localization in ferromagnetism of 3d transition metals, New J. Phys. 12 (2010) 063032, doi:10.1088/1367-2630/12/6/063032.
[11] J.P. Wang, N. Ji, X. Liu, Y. Xu, C. Sánchez-Hanke, Y. Wu, F.M.F. De Groot, L.F. Allard, E. Lara-Curzio, Fabrication of $Fe_{16}N_2$films by sputtering process and experimental investigation of origin of giant saturation magnetization in $Fe_{16}N_2$, IEEE Trans. Magn. (2012) 1710–1717, doi:10.1109/TMAG.2011.2170156.
[12] I. Dirba, C.A. Schwöbel, L.V.B. Diop, M. Duerrschnabel, L. Molina-Luna, K. Hofmann, P. Komissinskiy, H.-J. Kleebe, O. Gutfleisch, Synthesis, morphology, thermal stability and magnetic properties of α'' -$Fe_{16}N_2$ nanoparticles obtained by hydrogen reduction of γ -Fe_2O_3 and subsequent nitrogenation, Acta Mater. 123 (2017) 214–222, doi:10.1016/j.actamat.2016.10.061.
[13] H. Takahashi, M. Igarashi, A. Kaneko, H. Miyajima, Y. Sugita, Perpendicular uniaxial magnetic anisotropy of Fe/Sub 16/N/sub 2/[001]single crystal films grown by molecular beam epitaxy, IEEE Trans. Magn. 35 (1999) 2982–2984, doi:10.1109/20.801054.
[14] V. Zhukova, J.J. Val, M. Ilyn, M. Ipatov, R. Varga, C. Garcia, a. Zhukov, GMR effect in Co-Cu microwires, J. Korean Phys. Soc. 62 (2013) 1940–1944, doi:10.3938/jkps.62.1940.
[15] J.-P. Wang, Y. Jiang, A. Mehedi, J. Liu, α''-$Fe_{16}N_2$ compound based permanent magnet with 20MGOe magnetic energy product for next generation rare-earth-free magnet, in: Proceedings of the 24th International Workshop on Rare-Earth and Future Permanent Magnets and Their Application (REPM 2016), 2016, p. 1430.
[16] X. Li, M. Yang, M. Jamali, F. Shi, S. Kang, Y. Jiang, X. Zhang, H. Li, S. Okatov, S. Faleev, A. Kalitsov, G. Yu, P.M. Voyles, O.N. Mryasov, J. Wang, Heavy-Metal-Free, low-damping, and non-interface perpendicular $Fe_{16}N_2$ thin film and magnetoresistance device, Phys. Status Solidi Rapid. Res. Lett. 13 (2019) 1900089, doi:10.1002/pssr.201900089.
[17] K.H. Jack, The occurrence and the crystal structure of formula-iron nitride; a new type of interstitial alloy formed during the tempering of Nitrogen-Martensite, Proc. R. Soc. A Math. Phys. Eng. Sci. 208 (1951) 216–224, doi:10.1098/rspa.1951.0155.
[18] T. Burkert, L. Nordström, O. Eriksson, O. Heinonen, Giant magnetic anisotropy in tetragonal FeCo alloys, Phys. Rev. Lett. 93 (2004) 027203, doi:10.1103/PhysRevLett.93.027203.

[19] J. Liu, K. Schliep, S.H. He, B. Ma, Y. Jing, D.J. Flannigan, J.P. Wang, Iron nanoparticles with tunable tetragonal structure and magnetic properties, Phys. Rev. Mater. 2 (2018) 054415, doi:10.1103/PhysRevMaterials.2.054415.
[20] A. Nagatomi, S. Kikkawa, T. Hinomura, S. Nasu, F. Kanamaru, Synthesis of iron nitrides FexN (x: 2, 2-3, 4, 16/2) by nitrogenizing .ALPHA.-Fe in Ammonia Gas, and magnetic properties of the bulk sample of $Fe_{16}N_2$, J. Jpn. Soc. Powder Powder Metall. 46 (1999) 151–155, doi:10.2497/jjspm.46.151.
[21] T. Hattori, N. Kamiya, Y. Kato, Magnetic properties of $Fe_{16}N_2$ fine particles, J. Magn. Soc. Jpn. 25 (2001) 927–930, doi:10.3379/jmsjmag.25.927.
[22] R. Zulhijah, A.B. Dani Nandiyanto, T. Ogi, T. Iwaki, K. Nakamura, K. Okuyama, Gas phase preparation of spherical core–shell α''-$Fe_{16}N_2/SiO_2$ magnetic nanoparticles, Nanoscale 6 (2014) 6487, doi:10.1039/c3nr06867f.
[23] R. Zulhijah, A.B.D. Nandiyanto, T. Ogi, T. Iwaki, K. Nakamura, K. Okuyama, Effect of oxidation on α''-$Fe_{16}N_2$ phase formation from plasma-synthesized spherical core–shell α-Fe/Al_2O_3 nanoparticles, J. Magn. Magn. Mater. 381 (2015) 89–98, doi:10.1016/j.jmmm.2014.12.015.
[24] Y. Jiang, J. Liu, P.K. Suri, G. Kennedy, N.N. Thadhani, D.J. Flannigan, J.-P. Wang, Preparation of an α''-$Fe_{16}N_2$ Magnet via a ball milling and shock compaction approach, Adv. Eng. Mater. (2016) 18, doi:10.1002/adem.201500455.
[25] Y. Jiang, M. Al Mehedi, E. Fu, Y. Wang, L.F. Allard, J. Wang, Synthesis of $Fe_{16}N_2$ compound free-standing foils with 20MGOe magnetic energy product by nitrogen ion-implantation, Sci. Rep. 6 (2016) 25436, doi:10.1038/srep25436.
[26] O. Gutfleisch, M.A. Willard, E. Brück, C.H. Chen, S.G. Sankar, J.P. Liu, Magnetic materials and devices for the 21st century: stronger, lighter, and more energy efficient, Adv. Mater. 23 (2011) 821–842, doi:10.1002/adma.201002180.
[27] L. Liu, Z. Liu, M. Li, D. Lee, R.J. Chen, J. Liu, W. Li, A.R. Yan, Positive temperature coefficient of coercivity in Sm 1−x Dy x (Co 0.695 Fe 0.2 Cu 0.08 Zr 0.025) 7.2 magnets with spin-reorientation-transition cell boundary phases, Appl. Phys. Lett. 106 (2015) 052408, doi:10.1063/1.4907640.
[28] R.W. McCallum, L. Lewis, R. Skomski, M.J. Kramer, I.E. Anderson, Practical aspects of modern and future permanent magnets, Annu. Rev. Mater. Res. 44 (2014) 451–477, doi:10.1146/annurev-matsci-070813-113457.
[29] M.S. Walmer, C.H. Chen, M.H. Walmer, A new class of Sm-TM magnets for operating temperatures up to 550°C, IEEE Trans. Magn. 36 (2000) 3376–3381, doi:10.1109/20.908807.
[30] T. Ogawa, Y. Ogata, R. Gallage, N. Kobayashi, N. Hayashi, Y. Kusano, S. Yamamoto, K. Kohara, M. Doi, M. Takano, M. Takahashi, Challenge to the synthesis of α"-$Fe_{16}N_2$ compound nanoparticle with high saturation magnetization for rare earth free new permanent magnetic material, Appl. Phys. Express 6 (2013) 073007, doi:10.7567/APEX.6.073007.
[31] T. Kojima, S. Kameoka, M. Mizuguchi, K. Takanashi, A.-P. Tsai, FeNi and $Fe_{16}N_2$ magnets prepared using leaching, Mater. Trans. 60 (2019) 1066–1071, doi:10.2320/matertrans.M2019019.
[32] T. Ogi, A.B. Dani Nandiyanto, Y. Kisakibaru, T. Iwaki, K. Nakamura, K. Okuyama, Facile synthesis of single-phase spherical α''-$Fe_{16}N_2$ /Al_2O_3 core-shell nanoparticles via a gas-phase method, J. Appl. Phys. 113 (2013) 164301, doi:10.1063/1.4798959.
[33] C.W. Kartikowati, A. Suhendi, R. Zulhijah, T. Ogi, T. Iwaki, K. Okuyama, Effect of magnetic field strength on the alignment of α''-$Fe_{16}N_2$ nanoparticle films, Nanoscale 8 (2016) 2648–2655, doi:10.1039/C5NR07859H.
[34] W.P. Tong, N.R. Tao, Z.B. Wang, J. Lu, K. Lu, Nitriding iron at lower temperatures, Science 299 (80) (2003) 686–688, doi:10.1126/science.1080216.
[35] J. Liu, G. Guo, F. Zhang, Y. Wu, B. Ma, J.-P. Wang, Synthesis of α''-$Fe_{16}N_2$ ribbons with a porous structure, Nanoscale Adv. 1 (2019) 1337–1342, doi:10.1039/C9NA00008A.
[36] E.H.D.M. van Voorthuysen, D.O. Boerma, N.C. Chechenin, Low-temperature extension of the lehrer diagram and the iron-nitrogen phase diagram, Metall. Mater. Trans. A. 33 (2002) 2593–2598, doi:10.1007/s11661-002-0380-2.
[37] V.B. Trindade, R. Borin, B.Z. Hanjari, S. Yang, U. Krupp, H.-J. Christ, High-temperature oxidation of pure Fe and the ferritic steel 2.25Cr1Mo, Mater. Res. 8 (2005) 365–369, doi:10.1590/S1516-14392005000400002.
[38] Y. Watanabe, A. Nakano, A. Sato, Effect of magnetic fields on the formation of $Fe_{16}N_2$ precipitates in Fe-N alloys, Mater. Sci. Eng. A. 146 (1991) 151–160, doi:10.1016/0921-5093(91)90274-Q.
[39] Y. Jiang, V. Dabade, M.P. Brady, O. Rios, R.D. James, J.-P. Wang, 9 T high magnetic field annealing effects on Fen bulk sample, J. Appl. Phys. 115 (2014) 17A758, doi:10.1063/1.4868493.
[40] K. Ho, X. Xiong, J. Zhi, L. Cheng, Measurement of effective magnetic anisotropy of nanocrystalline Fe-Cu-Nb-Si-B soft magnetic alloys, J. Appl. Phys. 74 (1993) 6788–6790, doi:10.1063/1.355078.
[41] Y. Jing, Y. Xu, J.-P. Wang, Fabrication of Heuslar Fe[Sub 3]Si nanoparticles, J. Appl. Phys. 105 (2009) 07B520, doi:10.1063/1.3074135.
[42] J.V. Kasiuk, A.A. Maksimenko, J.A. Fedotova, M. Marszałek, S.K. Lazaruk, O.V. Kupreeva, Effect of the morphology on the mechanisms of the magnetization reversal of multilayered thin Co/Pd films, Phys. Solid State 58 (2016) 2312–2319, doi:10.1134/S1063783416110160.
[43] N.P. Suponev, R.M. Grechishkin, M.B. Lyakhova, Y.E. Pushkar, Angular dependence of coercive field in (Sm,Zr)(Co,Cu,Fe)z alloys, J. Mag. Mag. Mat. 157–158 (1996) 376–377.
[44] R. Alben, J.J. Becker, M.C. Chi, Random anisotropy in amorphous ferromagnets, J. Appl. Phys. 49 (1978) 1653–1658, doi:10.1063/1.324881.
[45] O. Akdogan, W. Li, B. Balasubramanian, D.J. Sellmyer, G.C. Hadjipanayis, Effect of exchange interactions on the coercivity of SmCo5 nanoparticles made by cluster beam deposition, Adv. Funct. Mater. 23 (2013) 3262–3267, doi:10.1002/adfm.201201353.
[46] M.D. Kuz'min, Shape of temperature dependence of spontaneous magnetization of ferromagnets: quantitative analysis, Phys. Rev. Lett. 94 (2005) 107204, doi:10.1103/PhysRevLett.94.107204.
[47] Y. Sugita, K. Mitsuoka, M. Komuro, H. Hoshiya, Y. Kozono, M. Hanazono, Giant magnetic moment and other magnetic properties of epitaxially grown Fe16N2 single-crystal films (invited), 70 (1991) 5977–5982.
[48] K. Sato, W. Schweika, P.H. Dederichs, H. Katayama-Yoshida, Low-temperature ferromagnetism in (Ga, Mn)N: ab initio calculations, Phys. Rev. B. 70 (2004) 201202, doi:10.1103/PhysRevB.70.201202.